Lorentz-force gyrator based on AlScN piezoelectric thin film

ⓘ Shuai Shao, ⓘ Zhifang Luo, ⓘ Kangfu Liu, et al.

COLLECTIONS

Paper published as part of the special topic on Piezoelectric Thin Films for MEMS

View Online   Export Citation   CrossMark

ARTICLES YOU MAY BE INTERESTED IN

High In content nitride sub-micrometer platelet arrays for long wavelength optical applications
Applied Physics Letters **121**, 211105 (2022); https://doi.org/10.1063/5.0120723

Study of electrical transport properties of GaN-based side-gate heterostructure transistors
Applied Physics Letters **121**, 212107 (2022); https://doi.org/10.1063/5.0124626
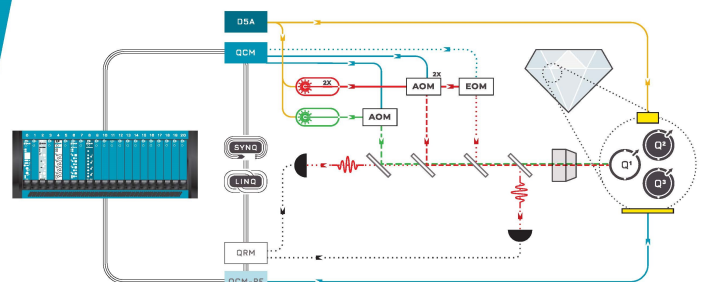
The universality of strength and plastic deformation in FCC concentrated solid solution (CSS) alloys at room and cryogenic temperatures
Applied Physics Letters **121**, 211901 (2022); https://doi.org/10.1063/5.0124716

AIP Publishing

Lorentz-force gyrator based on AlScN piezoelectric thin film

View Online   Export Citation   CrossMark

Shuai Shao,[1,2,3,a] Zhifang Luo,[1,2,3] Kangfu Liu,[1,2,3] and Tao Wu[1,2,3,4,a]

AFFILIATIONS

[1]School of Information Science and Technology, ShanghaiTech University, Shanghai 201210, China
[2]Shanghai Institute of Microsystem and Information Technology, Chinese Academy of Sciences, Shanghai 200050, China
[3]University of Chinese Academy of Sciences, Beijing 100049, China
[4]Shanghai Engineering Research Center of Energy Efficient and Custom AI IC, Shanghai 201210, China

Note: This paper is part of the APL Special Collection on Piezoelectric Thin Films for MEMS.
[a]Authors to whom correspondence should be addressed: shaoshuai@shanghaitech.edu.cn and wutao@shanghaitech.edu.cn

ABSTRACT

This paper reports a chip-scale radio frequency Lorentz-force gyrator based on an aluminum scandium nitride ($Al_{0.7}Sc_{0.3}N$) thin film. The two-port gyrator, which is essentially a lateral overtone bulk acoustic resonator, consists of a planar coil for Lorentz-force transduction and two top-bottom electrode pairs for piezoelectric transduction. The non-reciprocity is generated by the phase transition in the Lorentz-force coupling when an external vertical magnetic field is applied. The Lorentz-force gyrators based on both AlN and $Al_{0.7}Sc_{0.3}N$ thin films demonstrate good non-reciprocity, i.e., the 180° phase difference, at approximately 517 and 388 MHz, respectively. Thanks to larger piezoelectric constants, the $Al_{0.7}Sc_{0.3}N$ gyrator demonstrates easier impedance matching and a wider fractional bandwidth of 6.3% at a magnetic field of 1.65 T compared to 1.3% for an AlN device. Finally, an isolator consisting of the Lorentz-force gyrator and a shunt resistor is demonstrated over 35 dB of isolation and flat unidirectional transmission.

A non-reciprocal isolator and a circulator play important roles in the realization of radio frequency (RF) full-duplex communication.[1–3] Receiving and transmitting simultaneously on the same frequency band help double the efficiency of frequency resources utilization. Such non-reciprocal components can be constructed from a gyrator, which was proposed by Tellegen in 1948 as a non-reciprocal passive network unit.[4] Conventional non-reciprocal RF components are mainly realized by ferrite materials based on the magneto-optical Faraday effect.[5–8] A variety of new non-reciprocal devices have recently been demonstrated that can achieve the comparable performance as conventional ferrite devices.[9–14] Chip-scale passive MEMS gyrators draw great attention due to the advantages of miniature size and shorter acoustic wavelengths compared to electromagnetic waves. The size of such devices is correlated with the electromagnetic wavelength, which prevents the miniaturization and chip integration. Several types of chip-scale non-reciprocal devices have been demonstrated recently.[15–20] The multiferroic or magnetoelectric (ME) effect provides another approach to achieve non-reciprocity with large coupling coefficient.[21–28] However, the demand for high quality magnetostrictive thin film materials makes the chip-scale ME gyrator very

challenging. Alternatively, Lorentz-force based electromagnetic transduction could enable chip-scale non-reciprocal devices and has not been extensively studied.

A new type of the MEMS gyrator, as shown in Fig. 1(a), has been recently proposed utilizing a piezoelectric lateral overtone bulk acoustic resonator (LOBAR) and Lorentz-force hybrid transduction.[29] Two pairs of top/bottom electrodes serve as the piezoelectric transduction terminal (port 1), and a loop coil on top of the piezoelectric layer serves as the Lorentz-force transduction terminal (port 2). The conversion efficiency of the gyrator is determined by the piezoelectric and Lorentz-force transductions. By utilizing aluminum scandium nitride (AlScN), we present the chip-scale gyrator with large fractional bandwidth (FBW) and easy impedance matching as well as isolation application in RF communication and signal processing.

As illustrated in Fig. 1(a), the Lorentz-force gyrator design consists of a 1 μm $Al_{0.7}Sc_{0.3}N$ thin film plate of 210 μm long and 70 μm wide, and 100 nm Pt as the bottom electrodes and 200 nm Al above as the top electrodes and coil. The cross section in Fig. 1(a) indicates the displacement in the x-direction from finite element analysis. For optimized driving efficiency, the piezoelectric transducer of 10 μm in width
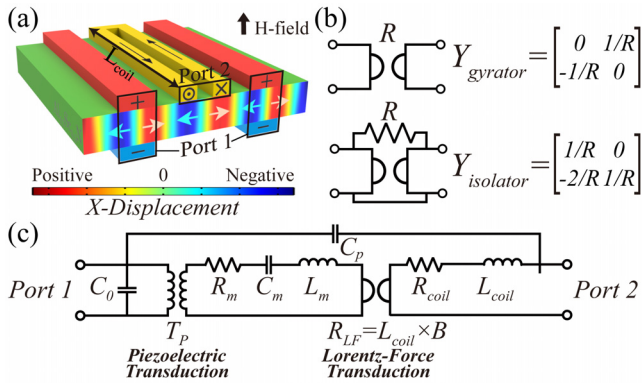
FIG. 1. (a) Schematic of an $Al_{0.7}Sc_{0.3}N$-based Lorentz-force gyrator. The cross section shows the x displacement. (b) The ideal impedance matrix for the gyrator and isolator. (c) The equivalent circuit model of the Lorentz-force gyrator.

and the coil of $5\,\mu m$ in width are configured at the point of maximum stress and displacement on the seventh-order LOBAR, respectively. The piezoelectric terminal (port 1) excites the seventh-order lateral overtone mode, causing a lateral displacement of the coil. With the help of a vertical magnetic field, a current of 90° leading phase is generated at the coil (port 2) by Faraday's law of electromagnetic induction. Conversely, the coil generates a Lorentz-force under the magnetic field and excites the same LOBAR mode, and the two pairs of electrodes collect the charge from the piezoelectric effect, which also comes with a 90° phase delay. Therefore, a non-reciprocity of 180° phase difference is, consequently, established between two ports. Figure 1(b) illustrates the admittance matrix of the ideal gyrator and isolator topology.

Figure 1(c) shows the equivalent circuit model of the Lorentz-force gyrator. C_0 is the static capacitance of the piezoelectric port, while C_p indicates the parasitic capacitance between the two ports.

The inductance and resistance of the coil port are represented by L_{coil} and R_{coil}, respectively. The ideal transformer and gyrator represent the piezoelectric transduction and Lorentz-force transduction with coupling coefficients of T_P and R_{LF}, respectively. L_{coil} is the longitudinal length of the coil, and B is the applied magnetic flux density. R_m, C_m, and L_m are the damping, spring, and equivalent mass of the LOBAR in the mechanical domain, respectively.

The transfer admittances of the Lorentz-force gyrator as a two-port passive device can be expressed as

$$Y_{transfer} = \pm \frac{1}{\left(R_m + \frac{1}{j\omega C_m} + j\omega L_m\right)\frac{(R_{coil} + j\omega L_{coil})}{T_P R_{LF}} + T_P R_{LF}} + j\omega C_p, \quad (1)$$

where R_{LF} is determined by the magnetic flux density times the coil length and T_P is primarily determined by the piezoelectric constant e_{31}. The equivalent circuit model can be divided into two branches with two resonances. The first one determined by C_m and L_m is the LOBAR mechanical resonant frequency. The other is the parallel resonance due to parasitic capacitance C_p. The magnetoelectric coupling coefficient of the Lorentz-force gyrator determines the non-reciprocal bandwidth, which can be derived as

$$ME_{coupling} = \frac{\pi^2}{8}\left(1 - \left(1 + \frac{\frac{\pi^2}{8}C_0 k_t^2}{C_p}\frac{T_P R_{LF}}{(R_{coil} + j\omega L_{coil})}\right)^{-1}\right). \quad (2)$$

The Sc doping in the $Al_{0.7}Sc_{0.3}N$ thin film improves both the efficiency of piezoelectric transduction T_P, by increasing the piezoelectric coefficients, and the motional capacitance C_m by lowering Young's modulus. Therefore, the gyrator ME coupling can be significantly improved compared to an AlN device with the same design.
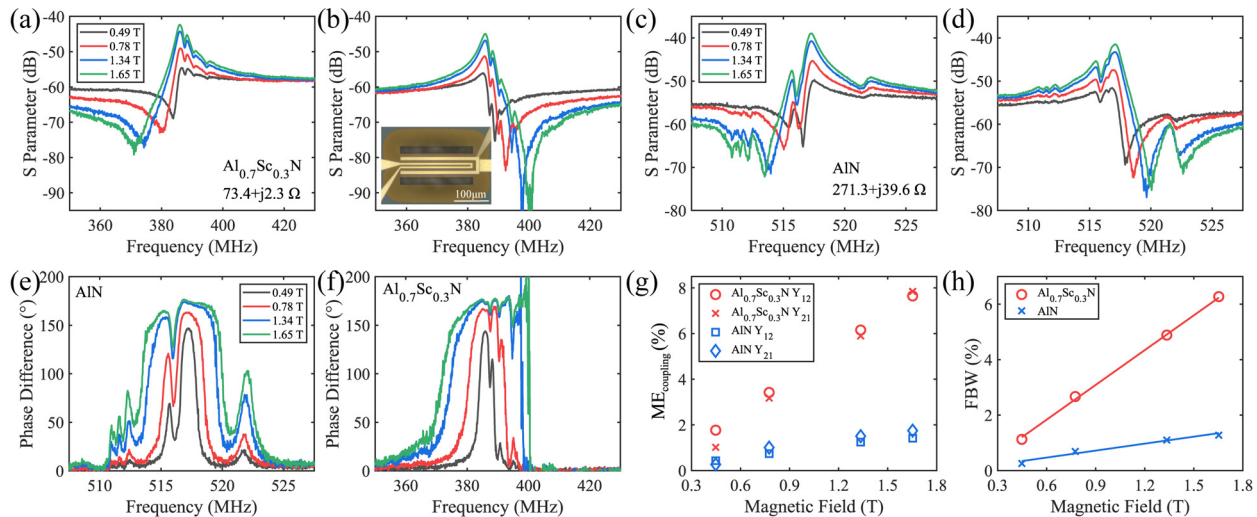

FIG. 2. (a) and (b) The S_{21} and S_{12} of the $Al_{0.7}Sc_{0.3}N$ Lorentz-force gyrator under different magnetic fields and (c) and (d) for the AlN device with the same design. Phase difference between the two ports for (e) AlN and (f) $Al_{0.7}Sc_{0.3}N$. (g) The ME coupling coefficients extracted from S-parameters and (h) gyration fraction bandwidth as a function of the external magnetic field.

TABLE I. Equivalent circuit model parameters of the AlN\Al$_{0.7}$Sc$_{0.3}$N gyrator.

	C_0 (pF)	C_m (nF)	L_m (pH)	R_m ($\mu\Omega$)
AlN	0.43	9.02	10.50	36.22
Al$_{0.7}$Sc$_{0.3}$N	1.12	17.65	9.51	80.23
R_{LF} (1.65 T)	T_P	C_p (fF)	L_{coil} (nH)	R_{coil} (Ω)
3.47×10^{-4}	3.74×10^{-4}	8.95	0.20	10.93
3.47×10^{-4}	9.01×10^{-4}	12.90	0.21	8.61

The fabricated Lorentz-force gyrator with the Al$_{0.7}$Sc$_{0.3}$N thin film is shown in Fig. 2(b). The fabrication process based on Al$_{0.7}$Sc$_{0.3}$N of the devices has been reported in Ref. 30. The same design based on AlN is also fabricated for comparison. A vector network analyzer is used to characterize the spectrum of the gyrator under the vertical magnetic fields in the range of 0.49–1.65 T.

Figures 2(a)–2(d) demonstrate matched S$_{21}$ and S$_{12}$ based on Al$_{0.7}$Sc$_{0.3}$N and AlN gyrators, respectively. With a wavelength of 20 μm, the AlN and Al$_{0.7}$Sc$_{0.3}$N gyrators operate at the resonant frequencies of 517 and 388 MHz, respectively. As the magnetic field increases, the maximum magnitudes of S$_{21}$ and S$_{12}$ increase. Port 1 of the Al$_{0.7}$Sc$_{0.3}$N gyrator is matched to $73.4 + j2.3$ Ω, while the AlN gyrator is matched to $271.3 + j39.6$ Ω, indicating easier impedance matching for the Al$_{0.7}$Sc$_{0.3}$N thin film device due to improved coupling. The parallel resonance frequencies of S$_{21}$ and S$_{12}$ appear on each side of the mechanical resonance, which is consistent with Eq. (1). The parameters extracted by the equivalent circuit are summarized in Table I.

Figures 2(e) and 2(f) show the gyration phase difference between S$_{12}$ and S$_{21}$ using AlN and Al$_{0.7}$Sc$_{0.3}$N, respectively. The gyrator bandwidth, defined as the frequency range with a phase difference of 180°, increases with external magnetic fields, which also agrees with the coupling coefficient trend under different magnetic fields as shown in Fig. 2(g). In addition, Sc doping increases piezoelectric transduction T$_P$ from 3.74×10^{-4} to 9.01×10^{-4}. Furthermore, Fig. 2(h) indicates that the FBW of the AlN gyrator increases from 0.3% to 1.3%, and 1.1% to 6.3% for Al$_{0.7}$Sc$_{0.3}$N as the magnetic field increases from 0.45 to 1.65 T.

Figures 3(a) and 3(b) show the S-parameter of the equivalent circuit simulation with the extracted parameters in Table I, which is a good fitting in comparison with experimental data shown in Fig. 2. The difference between the minimum values in S$_{21}$ and S$_{12}$ is mainly caused by L$_{coil}$. Currently, the devices still have large insertion loss. However, in the future, the loss can be significantly reduced by increasing the coil length, arranging the coil under the film, and improving the piezoelectric coupling to make the gyrator more suitable for practical applications.

Figure 3(c) illustrates the S-parameters of the isolation consisting of Al$_{0.7}$Sc$_{0.3}$N and AlN gyrators using topology in Fig. 1(b) at 1.65 T. Resistances of 1690 and 2734 Ω are used to obtain the maximum isolation. Over 35 dB isolation is achieved at 388.4 and 517.0 MHz with a minimum loss of -34.8 and -37.7 dB for both devices. The Al$_{0.7}$Sc$_{0.3}$N isolator benefits from impedance match with port 1 matched to $50.8 + j2.3$ Ω, comparing with the AlN device matched to $257.4 + j22.7$ Ω. Finally, the isolation and the parallel resistance vs magnetic field are shown in Fig. 3(d). The blue line shows the isolation when using the same 1690 Ω resistance. As the magnetic field increases, the AlScN gyrator can obtain a significantly better isolation
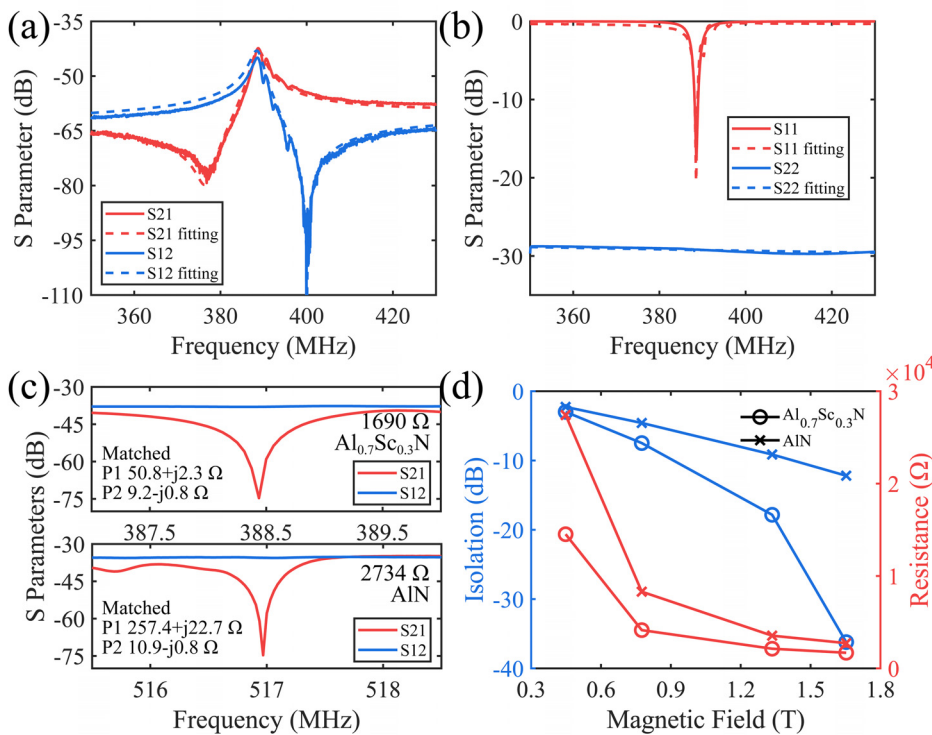

FIG. 3. (a) S$_{21}$ and S$_{12}$ and (b) S$_{11}$ and S$_{22}$ of the equivalent circuit simulation using the extracted parameters with Al$_{0.7}$Sc$_{0.3}$N. (c) S-parameters of the isolators consisting of the AlScN and AlN gyrators. Both ports are matched to 50 Ω. (d) Isolation of different magnetic fields with the same 1690 Ω and resistance for the maximum isolation.

than AlN. As the magnetic field reaches 1.65 T, the isolation of AlScN and AlN is 36.2 and 12.2 dB, respectively. Regarding the parallel resistance in red line, AlScN requires approximately only 60% of the resistance of AlN to obtain an equivalent isolation with lower loss.

In this work, we demonstrated the chip-scale large FBW Lorentz-force gyrator using the $Al_{0.7}Sc_{0.3}N$ thin film. Non-reciprocal 180° phase difference is obtained by Lorentz-force transduction. The gyrator demonstrates a gyration FBW of 6.3% at a center frequency of 388 MHz, which is 4.8 times larger compared to the pure AlN gyrator at the same magnetic field. Our results illustrate that the $Al_{0.7}Sc_{0.3}N$ thin film based Lorentz-Force gyrators will facilitate the establishment of non-reciprocity at smaller magnetic fields while providing greater bandwidth for RF communication and signal processing applications.

AUTHOR DECLARATIONS
Conflict of Interest

The authors have no conflicts to disclose.

Author Contributions

S.S. designed, optimized, and performed the device and conducted the experiments and simulations. Z.L. also conducted the film deposition and experiments. K.L. conducted the analysis and manuscript editing. T.W. conceived and supervised the research.

Shuai Shao: Conceptualization (equal); Data curation (equal); Formal analysis (equal); Writing – original draft (equal); Writing – review & editing (equal). **Zhifang Luo:** Data curation (equal); Formal analysis (equal). **Kangfu Liu:** Writing – review & editing (supporting). **Tao Wu:** Conceptualization (equal); Resources (equal); Supervision (equal); Writing – review & editing (equal).

DATA AVAILABILITY

The data that support the findings of this study are available within the article.

REFERENCES

[1]D. Bharadia, E. McMilin, and S. Katti, in Proceedings of the ACM SIGCOMM Conference on SIGCOMM (Association for Computing Machinery, 2013), pp. 375–386.

[2]J. Zhou, N. Reiskarimian, J. Diakonikolas, T. Dinc, T. Chen, G. Zussman, and H. Krishnaswamy, IEEE Commun. Mag. **55**, 142 (2017).

[3]A. Sabharwal, P. Schniter, D. Guo, D. W. Bliss, S. Rangarajan, and R. Wichman, IEEE J. Sel. Areas Commun. **32**, 1637 (2014).

[4]B. D. Tellegen, Philips Res. Rep. **3**, 81 (1948).

[5]C. E. Fay and R. L. Comstock, IEEE Trans. Microwave Theory Tech. **13**, 15 (1965).

[6]M. Pardavi-Horvath, J. Magn. Magn. Mater **215–216**, 171 (2000).

[7]E. N. Skomal, IEEE Trans. Microwave Theory Tech. **11**, 117 (1963).

[8]V. G. Harris, IEEE Trans. Magn. **48**, 1075 (2012).

[9]N. Reiskarimian and H. Krishnaswamy, Nat. Commun. **7**, 11217 (2016).

[10]D. L. Sounas, C. Caloz, and A. Alù, Nat. Commun. **4**, 2407 (2013).

[11]N. A. Estep, D. L. Sounas, J. Soric, and A. Alù, Nat. Phys. **10**, 923 (2014).

[12]M. Kostylev, J. Appl. Phys. **113**, 053907 (2013).

[13]A. Palermo, P. Celli, B. Yousefzadeh, C. Daraio, and A. Marzani, J. Mech. Phys. Solids **145**, 104181 (2020).

[14]H. Mansoorzare and R. Abdolvand, IEEE Electron Device Lett. **41**, 1444 (2020).

[15]M. M. Torunbalci, T. J. Odelberg, S. Sridaran, R. C. Ruby, and S. A. Bhave, IEEE Microwave Wireless Compon. Lett. **28**, 395 (2018).

[16]G. Michetti, C. Cassella, F. Pop, A. Pirro, A. Kord, D. Sounas, A. Alú, and M. Rinaldi, in IEEE International Ultrasonics Symposium (IUS) (IEEE, 2018), pp. 206–212.

[17]S. Ghosh and M. Ricci, in Joint Conference of the IEEE International Frequency Control Symposium & IEEE International Symposium on Applications of Ferroelectrics (IFCS-ISAF) (IEEE, 2020).

[18]R. Lu, T. Manzaneque, Y. Yang, L. Gao, A. Gao, and S. Gong, IEEE Trans. Microwave Theory Tech. **67**, 1516 (2019).

[19]H. Tian, J. Liua, A. Siddharth, R. N. Wang, T. Blésin, J. He, T. J. Kippenberg, and S. A. Bhave, in Conference on Lasers Electro-Optics (CLEO) (2021).

[20]R. Lu, J. Krol, L. Gao, and S. Gong, Sci. Rep. **8**, 14655 (2018).

[21]J. Zhang, B. Ge, Q. Zhang, D. A. Filippov, J. Wu, J. Tao, Z. Jia, L. Jiang, L. Cao, and G. Srinivasan, Appl. Phys. Lett. **118**, 042402 (2021).

[22]X. Zhuang, C. M. Leung, G. Sreenivasulu, M. Gao, J. Zhang, G. Srinivasan, J. Li, and D. Viehland, Appl. Phys. Lett. **111**, 163902 (2017).

[23]C. M. Leung, X. Zhuang, D. Friedrichs, J. Li, R. W. Erickson, V. Laletin, M. Popov, G. Srinivasan, and D. Viehland, Appl. Phys. Lett. **111**, 122904 (2017).

[24]J. Zhai, J. Li, S. Dong, D. Viehland, and M. I. Bichurin, J. Appl. Phys. **100**, 124509 (2006).

[25]C. M. Leung, G. Sreenivasulu, X. Zhuang, X. Tang, M. Gao, J. Xu, J. Li, J. Zhang, G. Srinivasan, and D. Viehland, Phys. Status Solidi RRL **12**, 1800043 (2018).

[26]C. Tu, C. Dong, Z. Chu, H. Chen, X. Liang, and N. X. Sun, Appl. Phys. Lett. **113**, 262904 (2018).

[27]J. Zhai, J. Gao, C. De Vreugd, J. Li, D. Viehland, A. V. Filippov, M. I. Bichurin, D. V. Drozdov, G. A. Semenov, and S. X. Dong, Eur. Phys. J. B **71**, 383 (2009).

[28]C.-W. Nan, M. I. Bichurin, S. Dong, D. Viehland, and G. Srinivasan, J. Appl. Phys. **103**, 031101 (2008).

[29]T. Wu, R. Lu, A. Gao, C. Tu, T. Manzaneque, and S. Gong, in IEEE 32nd International Conference on Micro Electro Mechanical Systems (MEMS) (IEEE, 2019), pp. 887–890.

[30]S. Shao, Z. Luo, and T. Wu, IEEE Electron Device Lett. **42**, 1378 (2021).